View metadata, citation and similar papers at core.ac.uk
brought to you by CORE
provided by University of East Anglia digital repository

Longan seed- and mangosteen skin-based activated carbons for the removal of Pb(II) ions and Rhodamine-B dye from aqueous solutions

Xiaoting Hong [a,*], Chengran Fang [a], Mengxian Tan [b], Haifeng Zhuang [a], Wanpeng Liu [a], K.S. Hui [c], Zhuoliang Ye [d,*], Shengdao Shan [a], Xianghong Lü [b]

[a] *School of Civil Engineering and Architecture, Zhejiang University of Science and Technology; Key Laboratory of Recycling and Eco-treatment of Waste Biomass of Zhejiang Province, Hangzhou 310023, China*

[b] *School of Chemistry & Environment, South China Normal University, Guangzhou 510006, China*

[c] *School of Mathematics, University of East Anglia, Norwich, NR4 7TJ, United Kingdom*

[d] *School of Chemical Engineering, Fuzhou University, Fuzhou, Fujian 350116, P. R. China*

∗ Corresponding author. Tel.: +86 571 85070528; fax: +86 571 85070143.

E-mail address: hanren.xiaoting@gmail.com (X.T. Hong); yezl@fzu.edu.cn (Z. Ye).

All e-mails:

Dr Xiaoting Hong, hongxt@zust.edu.cn

Dr Chengran Fang, fangchengr@163.com

Miss Mengxian Tan, tanxumong@foxmail.com

Dr Haifeng Zhuang, 286339399@qq.com

Dr Wanpeng Liu, wpliu@zust.edu.cn

Dr K.S. Hui, k.hui@uea.ac.uk

Dr Zhuoliang Ye, yezl@fzu.edu.cn

Dr Shengdao Shan, shanshd@vip.sina.com

Dr Xianghong Lü, 173063369@qq.com

Abstract:

Agricultural biomass wastes of longan seeds and mangosteen skins were collected for precursors to prepare activated carbon through medium-temperature carbonization and KOH activation at high temperature. Pore structure, structural properties, and surface morphology were characterized by X-ray diffraction, Brunauer–Emmett–Teller surface measurement, and scanning electron microscopy. Effects of contact time and pH on the adsorption performances of samples were investigated by the remediation of lead and Rhodamine-B from aqueous solution. The experimental adsorption isotherms of Rhodamine-B and Pb(II) ions on LS-AC-5 and MS-AC-5 well fitted the Langmuir model. Results further showed that MS-AC-5 had a larger surface area of 2960.56 m^2/g and larger portion of micropore and mesopore (1.77 cm^3/g) than LS-AC-5 (2728.98 m^2/g and 1.39 cm^3/g, respectively). The maximum monolayer adsorption capability (1265.82 and 117.65 mg/g) of Rhodamine-B and Pb(II) ions on MS-AC-5 were higher than those on LS-AC-5 (543.48 and 107.53 mg/g, respectively).

1. Introduction

The rapid growth of developing countries has accelerated the process of water pollution. Millions of tons of wastewater discharged by mills each year contain chemicals, such as heavy metals and dyes. These chemicals, which are a problem affecting economic and ecological system around the world, cause both environmental damage and human disease. Various treatment techniques have been used to control the effluents released from mills, such as adsorption [1], membrane filtration [2], ion exchange [3], reverse osmosis [4], advanced oxidation [5], electrochemical methods, precipitation, and coagulation techniques [6]. However, these methods differ in their efficiency, cost, and environmental impact. Adsorption has long been considered as a highly efficient approach for pollution control. The main adsorption mechanisms are based on surface forces, complexation, and ion exchange mechanisms [7]. Various adsorbents, such as carbon-based nanomaterials [8], zeolite [9], resin [10], MOFs [11], clay minerals [12], and porous silica [13], have been developed for the removal of contaminants from wastewater due to the availability of various types and their high efficiency in removal of organic and inorganic pollutants.

Among all the adsorbents, nanostructured porous carbons are of great interest in view of their large surface areas, well-developed pore structures, surface properties, high adsorbing capacity, eco-friendly, cost feasibility, and excellent thermochemical stability. Porous carbons obtained from agricultural biowastes are attracting considerable attention due to the fact that agricultural wastes are recyclable, inexpensive, and abundantly available compared with non-renewable coal-based activated carbons. Besides the inherent advantages of abundance and low cost, agricultural biowastes mainly consisting of cellulose, lignin, and hemicelluloses also render them good sources of raw materials for the production of activated carbon adsorbents. The utilization of biomass waste for producing porous carbon simultaneously offers a solution for comprehensive and high-value utilization and approving the agricultural waste management. Several research have been reported on porous carbon materials from agricultural wastes, including coconut shell, seaweeds,

corn cob, rice husk, palm shell, tree leaves, bamboo debris, sugarcane bagasse, fish scale, animal bone, chicken feather, and so on [14–17].

The lead pollution in wastewater originates mostly from mining, smelting, lead-acid batteries manufacturing, metal plating and finishing, printing, ceramics, and glass industries. In the past episodes, significant concerns have been raised over lead contamination in the aquatic environment and the awareness about their toxicity has been dramatically increased. Lead has been proved to be one of the most toxic heavy metals and classified as a human carcinogen with permissible level of 0.015 mg/L in drinking water [18]. Therefore, to develop effective activated carbon absorbents to eliminate lead ions from wastewaters is of great demand. Papaya peel was utilized to prepare a novel activated carbon showing a high adsorption capacity for 200 mg/L Pb(II) with a removal rate of 93% in 2 h, where the adsorption data were consistent with both Langmuir and Freundlich adsorption models [19]. Sugarcane bagasse was combined with sludge to produce a low-cost porous carbon adsorbent successively through KOH activation and HNO_3 oxidation for Pb(II) ions with great adsorption capacity [20]. Three activated carbon samples produced from guava seeds, tropical almond shells, and dindé stones were investigated for the remediation of lead from water with a maximum amount of lead adsorbed as high as 50 mg/g (dindé stones), 96 mg/g (gava seeds), and 112 mg/g (almond shells), respectively [21]. Olive stone-derived microporous activated carbon is of largest adsorption capacity for removing Pb(II) in comparison with Cu(II) and Cd(II) from single and binary aqueous solutions via the batch technique [22].

Rhodamine-B is a cationic xanthene dye widely used as a colorant in the printing, textile dyeing, paint industries, and photographic industries [23]. However, this dye inherently possesses carcinogenicity, neurotoxicity, chronic toxicity, and reproductive toxicity towards humans and animals [24]. Thus, treating dyeing wastewater and solving water pollution are important. Although dyes in wastewater are difficult to remove due to their complex composition and inert properties, activated carbon adsorption is a particularly effective approach. Activated carbons were developed from a low-cost aquatic plant residue of *Lythrum salicaria* L. and tested for their

ability to remove rhodamine-B from aqueous solutions, where the maximum adsorption capacity derived from Langmuir model reached a value of 384.62 mg/g [25]. The by-products from woody biomass gasification were also utilized to prepare activated carbon via steam activation for the adsorption of Rhodamine-B dye. The adsorption isotherms well fit the Langmuir model with a maximum monolayer adsorption capability of 189.83 mg/g [26]. Similarly, rice husk-based activated carbon was also shown to be a promising adsorbent for removal of Rhodamine-B from aqueous solution and exhibited maximum monolayer adsorption capacity 518.1 mg/g [27].

The present study aims to produce activated carbon from agricultural biowastes of longan seed and mangosteen skin by KOH activation for the remediation of lead and Rhodamine-B from aqueous solution. The adsorption potential of two biomass-derived porous carbon for removal of lead and Rhodamine-B was evaluated in terms of the physicochemical characteristics of the porous carbon and the operating conditions. Finally, the adsorption equilibrium was also explored and fitted by Langmuir adsorption model.

2. Materials and methods

2.1. Materials

Chemical reagents that were used in this study were available commercially. KOH (AR; ≥85.0% purity) and HNO_3 (AR; 65%) were purchased from Tianjin Kemiou Chemical Reagent Co., Ltd. Longan seed and mangosteen skin were collected from a fruit trading center at Guangzhou.

2.2. Synthesis of activated carbons

Longan seed and mangosteen skin were firstly washed by deioinized water, then dried at 105 °C in an oven for 24 h and finally pulverized to biomass powders by an electric pulverizer. The resultant agricultural biomass powders were then transferred into corundum boats preliminarily heated by an atmosphere tubular furnace to the target temperature 450 °C at a heating rate of 3 °C/min under Ar atmosphere (flow

rate of 20 mL/min) and held at 450 °C for 120 min. The as-prepared biochar was gridded and then homogeneously mixed with solid KOH at different weight ratios (1:1, 1:4, and 1:5). Thereafter, the mixtures were loaded into a nickel combustion boat and activated in the Ar atmosphere furnace at 800 °C for 2 h with a heating rate of 3 °C/min and flow rate of 20 mL/min. Afterwards, the activated samples were alternatively washed several times with by 15% HNO_3 and deionized water to remove any inorganic salts or a residue KOH and dried at 110 °C for 12 h. Finally, the as-prepared activated porous carbons were denoted as LS-AC-*x* and MS-AC-*x*, separately, where LS and MS refer to longan seed and mangosteen skin, respectively; AC for activated carbon, x for the weight ratio of biochar to solid KOH.

2.3. Characterization methods

The X-ray diffraction (XRD) patterns were collected using a Bruker D8 advance diffractometer with monochromatic Cu Kα radiation (40 kV, 20 mA) covering 2θ regions from 10° to 80°. The specific surface area of the resultant porous carbons was obtained from N_2 adsorption–desorption isotherms on the Micromeritics ASAP 2020 Brunauer–Emmett–Teller (BET) apparatus at liquid nitrogen temperature (77 K). A hybrid nonlocal density functional theory (NLDFT) method was used to investigate the pore size distributions based on the N_2 adsorption isotherms by assuming slit pore geometry for the micropores and cylindrical pore geometry for the mesopores. The nanostructures of the longan seed- and mangosteen skin-derived porous carbons were investigated by field emission scanning electron microscopy (FE-SEM, ZEISS Ultra 55).

2.4. Adsorption experiments

The influence of time on the adsorption performance was carried out by adding 20 mg of LS-AC-5 and MS-AC-5 into 100 mL Rhodamine-B solution of 200 mg/L and Pb(II) solution of 10 mg/L under vigorous stirring, separately. The samples were taken at different time intervals in 120 min and analyzed by a UV/vis spectrophotometer (UV-1800, Shimadzu Corporation) at wavelength 554 nm and an atomic absorption

spectrophotometer (TAS-986, Beijing Persee Corporation) after filtration using 0.45 μm-syringe filters. The effect of the initial solution pH on the adsorption was evaluated by adjusting the initial pH solutions with 0.1 M KOH or 0.1 M HNO_3 to range within 3.0 to 9.0. Batch isotherm sorption experiments were performed by a series of adsorption using 100 mL Rhodamine-B solutions (20–2000) mg/L and 100 mL Pb(II) solutions (5–100 mg/L) in the presence of 20 mg of LS-AC-5 and MS-AC-5 under vigorous stirring, respectively. The concentrations of the samples were analyzed after 18 h. Langmuir model was used to simulate the adsorption processes. The Langmuir isotherm is applicable to monolayer adsorptions on energetically heterogeneous surface; it can be expressed as following Equation (1):

$$\frac{C_e}{Q_m} = \frac{C_e}{Q_e} + \frac{1}{Q_e K_L} \quad (1)$$

where Q_e (mg/g) is the equilibrium adsorption capacity, C_e (mg/L) is equilibrium concentration, Q_m (mg/g) is the maximum adsorption capacity, and K_L is equilibrium adsorption constant for Langmuir model.

3. Results and discussion

FE-SEM images of microstructures of LS-AC-1, LS-AC-4, LS-AC-5, MS-AC-1, MS-AC-4, and MS-AC-5 carbons are shown in Fig. 1. Figs. 1a and 1d show that at a low ratio of KOH to biochar, the porous carbons are dominated by macropores for the two types of porous carbons. For longan seed-derived porous carbons, a number of mesopores/micropores are generated in the nested cavities on the surfaces as the increasing ratios of KOH activating agent to biochar from Figs. 1a to 1c. However, mangosteen skin-derived porous carbons exhibit a different morphology that is featured by an increasing irregular nanosheet as the ratio of KOH to biochar increases as shown in Figs. 1d to 1f. These results indicate that a significant improvement of meso/microporous morphology has occurred in the KOH activation process which leads to a substantial number of porosity comprised of randomly oriented microspores or nanosheets.

Figure 2 shows the XRD patterns of the as-synthesized LS-AC-1, LS-AC-4, LS-AC-5, MS-AC-1, MS-AC-4, and MS-AC-5. As the ratio of KOH to carbon increases, the diffraction peaks located at 2θ=26° and 43° corresponding to (002) and (100) planes exhibit a reduced intensity and a broadened property; this result suggests that stronger activator leads to a higher percentage of amorphous structure due to the breakdown of graphitic crystalline structures during chemical activation.

As shown in Fig. 3, nitrogen adsorption–desorption isotherms were used to investigate the BET surface area and porosity of longan seed- and mangosteen skin-derived porous carbons. LS-AC-1, LS-AC-4, LS-AC-5, MS-AC-1, MS-AC-4, and MS-AC-5 exhibit type-I N_2 adsorption isotherm showing a steep nitrogen gas uptake at lower relative pressure ($P/P_0 < 0.01$) and a plateau in the intermediate pressure section; these results indicate that a microporous nature with a small degree of mesoporosity. Hybrid NLDFT model was used to determine the pore size distribution and total pore volumes by assuming cylindrical-pore geometry for the mesopores and slit-pore geometry for the micropores according to the N_2 isotherm adsorption data. Table 1 summarizes the specific surface area and pore structure of samples activated with different ratios of biochar to KOH. On one hand, for LS-AC, as the ratio of KOH to biochar was increased, the total pore volume increased from 0.47 cm^3/g to 1.39 cm^3/g, BET surface area increased from 803.51 m^2/g to 2728.98 m^2/g, and average pore size decreased from to 2.36 nm to 2.04 nm. On the other hand, for MS-AC, as the ratio of KOH to biochar was increased, the total pore volume increased from 0.51 cm^3/g to 1.77 cm^3/g, BET surface area increased from 940.24 m^2/g to 2960.56 m^2/g, and average pore size decreased from to 2.19 nm to 1.93 nm. These changes are attributed to presence of the more activating agents that are accessible to react with biochar to facilitate the formation of abundant micropores. All the samples exhibited a random pore size distribution with several representative peaks centering in the range of <5 nm. With increased percentage of activating agent, agricultural biomass-derived porous carbons contain a structure that is predominantly micropore with peaks center at 1.1, 0.5, and 1.2 nm for LS-AC-5 and MS-AC-5.

The removal rate (%) of Rhodamine-B and Pb(II) ions on LS-AC-5 and MS-AC-5

as a function of contact time is presented in Figs. 4a and 5a. The removal rate of Rhodamine-B was gradually increased with the adsorption time from 22.86% to 76.78% on LS-AC-5 and from 28.59% to 83.16% on MS-AC-5 in 120 min. Pb(II) ions was removed greatly from the aqueous solution at the beginning (<5 min) due to the high surface areas and large amount of unoccupied active sites (carboxyl and phenolic hydroxyl groups) on the porous carbons [28, 29]. Pb(II) ions adsorption from aqueous solutions by porous carbon was highly affected by solution pH. Figs. 4b and 5b show that adsorption capacity increased with increased pH in the range of 3.0–7.0. As pH increases, the porous carbon surface becomes more and more negatively charged within the pH range which favourably led to higher adsorption capacity of cationic charged Pb(II) ions via electrostatic interaction. Analogously, adsorption value was relatively low at pH of 3, which can be attributed to electrostatic repulsion between cationic charged Pb(II) ions and the hydrogen ions that were released from phenolic hydroxyl groups in the adsorption process. However, the pH of the solution slightly influences Rhodamine-B adsorption process with the exception at high pH of 9, which is inconsistent with adsorption behaviors on an adsorbent with very low surface area elsewhere [30], inferring that high surface area completely dominated during the adsorption compared to surface charge of the adsorbents. The comparison of adsorption isotherms of Rhodamine-B and Pb(II) ions on LS-AC-5 and MS-AC-5 is shown in Figs. 4c and 5c. In Figs. 4d and 5d, the plots show that the values of the Langmuir isotherm model well fit the experimental data with square of correlations higher than 0.999 indicating a monolayer coverage of adsorbent surface [31]. The isotherm parameters for the Langmuir isotherm model are listed in Table 2. The equilibrium adsorption capacity (Q_e, mg/g) of LS-AC-5 and for Rhodamine-B and Pb(II) ions are 543.48 and 107.53 mg/g, respectively, whereas that of MS-AC-5 are 1265.82 and 117.65 mg/g, respectively. The removal efficiency of Rhodamine-B and Pb(II) ions on MS-AC-5 was higher than that of LS-AC-5 because of higher surface area and pore volume.

4. Conclusions

Two types of activated carbons were prepared from fruit-biomass wastes by chemical activation with KOH. These activated carbons were characterized in terms of surface and structural properties and then used to remediate Rhodamine-B and Pb(II) in aqueous solutions. MS-AC had larger specific surface area, pore volume, and smaller average pore size than LS-AC. The experimental equilibrium curves of Rhodamine-B and Pb(II) on LS-AC-5 and MS-AC-5 well fitted the Langmuir isotherm model. MS-AC-5 had the highest adsorption capability for the removal of Rhodamine-B and Pb(II) ions from aqueous solutions, with maximum adsorption capacities of 1265.82 and 117.65 mg/g, which was mainly attributed to its higher surface area and more available micropore. The impact of solution pH on the adsorption amount of Pb(II) ions was markedly stronger than that of Rhodamine-B.

Acknowledgements Financial support for this work was provided by the National Key R&D Program of China (13th Five Year Plan, 2017YFD061006), Zhejiang University of Science and Technology Youth Talent Cultivation Plan, Major Science and Technology Projects of Zhejiang Province (2015C02037), and Fuzhou University Qishan Scholar [Oversea project, grant number XRC-1508].

References

[1] Wołowicz A, Hubicki Z (2016) Carbon-based adsorber resin Lewatit AF 5 applicability in metal ion recovery. Microporous and Mesoporous Materials 224:400-414.

[2] Habineza A, Zhai J, Ntakirutimana T, Qiu FP, Li X, Wang Q (2017) Heavy metal removal from wastewaters by agricultural waste low-cost adsorbents: hindrances of adsorption technology to the large scale industrial application – a review, Desalination and Water Treatment 78:18-214.

[3] Guergazi S, Hamzaoui S, Achour S (2017) Effect of the mineralization on removing the humic substances by adsorption on activated carbon Desalination and Water Treatment 78:127-131.

[4] Cakmakci M, Baspinar AB, Balaban U, Uyak V, Koyuncu I, Kinaci C (2009)

Comparison of nanofi ltration and adsorption techniques to remove arsenic from drinking water, Desalination and Water Treatment 9:149-154.

[5] Chi FH, Cheng WP, Tian DR, Yu RF, Fu CH (2015) Potassium alum crystal derived from aluminum salt in water treatment sludge by nanofiltration. Journal of Material Cycles and Waste Management 17:522-528.

[6] Abda MB, Schäf O, Zerega Y (2015) Ion exchange effect on asymmetric dioxins adsorption onto FAU-type X-zeolites, Microporous and Mesoporous Materials 217:178-183.

[7] Xu Z, Liu J, Huang Z, Yang X, Wang S, Fang F, Chen S., Wang Y (2017) Experimental study of a stand-alone solar-wind powered reverse osmosis seawater desalination system, Desalination and Water Treatment 78:24-33.

[8] Colla V, Branca TA, Rosito F, Lucca C, Vivas BP, Delmiro VM (2016) Sustainable Reverse Osmosis application for wastewater treatment in the steel industry, Journal of Cleaner Production 130:103-115.

[9] Zhang C, Jin M, Tang J, Gao X (2016) Removal of cyclic volatile methylsiloxanes in effluents from treated landfill leachate by electrochemical oxidation, Journal of Material Cycles and Waste Management 2016:1-5.

[10] Ginni M, Kumar SA, Banu JR, Yeom IT (2017) Synergistic photodegradation of pulp and paper mill wastewater by combined advanced oxidation process, 68:160-169.

[11] Silva LF, Barbosa AD, Paula HM, Romualdo LL, Andrade LS (2016) Treatment of paint manufacturing wastewater by coagulation/electrochemical methods: Proposals for disposal and/or reuse of treated water, Water Research 101:467-475.

[12] Peng X, Hu F, Lam FLY, Wang Y, Liu Z, Dai H (2015) Adsorption behavior and mechanisms of ciprofloxacin from aqueous solution by ordered mesoporous carbon and bamboo-based carbon, Journal of Colloid and Interface Science 460:349-360.

[13] Chan WH, Mazlee MN, Ahmad ZA, Ishak MAM, Shamsul JB (2015) The development of low cost adsorbents from clay and waste materials: a review, Journal of Material Cycles and Waste Management 2015:1-14.

[14] Li K, Wan Z, Li J, Lu M, Wang X (2017) Amino-functionalized bimodal ordered

mesoporous carbon with high surface area for efficient adsorption of lead (II) ions, 60:200-211.

[15] Yam LW, Lim L, Hosseini S, Choong TSY (2016) Enhancement of phenol adsorption on mesoporous carbon monolith modified by NaOH and NH_3: equilibrium and kinetic studies, 57:4183-4193.

[16] Tahri N, Jedidi I, Ayadi S, Cerneaux S, Cretin M, Amar RB (2016) Preparation of an asymmetric microporous carbon membrane for ultrafiltration separation: application to the treatment of industrial dyeing effluent, 57:23473-23488.

[17] Wang L, Han C, Nadagouda MN, Dionysiou DD (2016) An innovative zinc oxide-coated zeolite adsorbent for removal of humic acid, Journal of Hazardous Materials 313:283-290.

[18] Li K, Liang H, Qu F, Shao S, Yu H, Han Z, Du X, Li G (2014) Control of natural organic matter fouling of ultrafiltration membrane by adsorption pretreatment: Comparison of mesoporous adsorbent resin and powdered activated carbon, Journal of Membrane Science 471:94-102.

[19] Yin N, Wang K, Wang L, Li Z (2016) Amino-functionalized MOFs combining ceramic membrane ultrafiltration for Pb (II) removal, Chemical Engineering Journal 306:619-628.

[20] Lyu Y, Su X, Zhang S, Zhang Y (2016) Preparation and Characterization of La(III)-Al(III) Co-loaded Hydrothermal Palygorskite Adsorbent for Fluoride Removal from Groundwater, Water, Air, & Soil Pollution 2016: 227:454.

[21] Liu F, Wu Z, Wang D, Yu J, Jiang X, Chen X (2016) Magnetic porous silica–graphene oxide hybrid composite as a potential adsorbent for aqueous removal of p-nitrophenol, Colloids and Surfaces A: Physicochemical and Engineering Aspects 490:207-214.

[22] Hong XT, Hui KS, Zeng Z, Hui KN, Zhang L, Mo M, Li M (2014) Hierarchical nitrogen-doped porous carbon with high surface area derived from endothelium

corneum gigeriae galli for high-performance supercapacitor, Electrochimica Acta 130:464-469.

[23] Bhatnagar A, Kaczala F, Hogland W, Marques M, Paraskeva CA, Papadakis VG, Sillanpää M (2014) Valorization of solid waste products from olive oil industry as potential adsorbents for water pollution control—a review, Environmental Science and Pollution Research 21:268-298.

[24] Garba A, Nasri NS, Basri H, Ismail R, Majid ZA, Hamza UD, Mohammed J (2016) Adsorptive removal of phenol from aqueous solution on a modified palm shell based carbon: fixed-bed adsorption studies, 57:29488-29499.

[25] Demiral I, Samdan CA, Demiral H (2016) Production and characterization of activated carbons from pumpkin seed shell by chemical activation with $ZnCl_2$, 57:2446-2454.

[26] Mohanraj N, Bhuvaneshwari S (2017) Decolorization of eosin-Y dye using activated carbon electrode prepared from bael fruit (Aegle marmelos) shell, 65:233-242.

[27] Liu H, Dai P, Zhang J, Zhang C, Bao N, Cheng C, Ren L (2013) Preparation and evaluation of activated carbons from lotus stalk with trimethyl phosphate and tributyl phosphate activation for lead removal, Chemical Engineering Journal 228:425-434.

[28] Abbaszadeh S, Alwi SRW, Webb C, Ghasemi N, Muhamad II (2016) Treatment of lead-contaminated water using activated carbon adsorbent from locally available papaya peel biowaste, Journal of Cleaner Production 118:210-222.

[29] Tao HC, Zhang HR, Li JB, Ding WY (2015) Biomass based activated carbon obtained from sludge and sugarcane bagasse for removing lead ion from wastewater, Bioresource Technology 192:611-617.

[30] Largitte L, Brudey T, Tant T, Dumesnil PC, Lodewyckx P (2016) Comparison of the adsorption of lead by activated carbons from three lignocellulosic precursors, Microporous and Mesoporous Materials 219:265-275.

[31] Bohli T, Ouederni A, Fiol N, Villaescusa I (2015) Evaluation of an activated carbon from olive stones used as an adsorbent for heavy metal removal from aqueous

phases, Comptes Rendus Chimie 18:88-99.

[32] Das M, Bhattacharyya KG (2014) Oxidation of Rhodamine B in aqueous medium in ambient conditions with raw and acid-activated MnO_2, NiO, ZnO as catalysts, Journal of Molecular Catalysis A: Chemical 391:121-129.

[33] Nagaraja R, Kottam N, Girija CR, Nagabhushana BM (2012) Photocatalytic degradation of Rhodamine B dye under UV/solar light using ZnO nanopowder synthesized by solution combustion route, Powder Technology 216:91-97.

[34] Huang Y, Zheng X, Feng S, Guo Z, Liang S (2016) Enhancement of rhodamine B removal by modifying activated carbon developed from Lythrum salicaria L. with pyruvic acid, Colloids and Surfaces A: Physicochemical and Engineering Aspects 489:154-162.

[35] Maneerung T, Liew J, Dai Y, Kawi S, Chong C, Wang CH (2016) Activated carbon derived from carbon residue from biomass gasification and its application for dye adsorption: Kinetics, isotherms and thermodynamic studies, Bioresource Technology 200:350-359.

[36] Ding L, Zou B, Gao W, Liu Q, Wang Z, Guo Y, Wang X, Liu Y (2014) Adsorption of Rhodamine-B from aqueous solution using treated rice husk-based activated carbon, Colloids and Surfaces A: Physicochemical and Engineering Aspects 446:1-7.

[37] S. Yao, J. Zhang, D. Shen, R. Xiao, S. Gu, M. Zhao, J. Liang, Removal of Pb(II) from water by the activated carbon modified by nitric acid under microwave heating, Journal of Colloid and Interface Science, 463 (2016) 118-127.

[38] Barczak M, Michalak-Zwierz K, Gdula K, Tyszczuk-Rotko K, Dobrowolski R, Dąbrowski A (2015) Ordered mesoporous carbons as effective sorbents for removal of heavy metal ions, Microporous and Mesoporous Materials 211:162-173.

[39] Inyinbor AA, Adekola FA, Olatunji GA (2016) Kinetics, isotherms and thermodynamic modeling of liquid phase adsorption of Rhodamine B dye onto Raphia hookerie fruit epicarp, Water Resources and Industry 15:14-27.

[40] Zhu R, Chen Q, Zhou Q, Xi Y, Zhu J, He H (2016) Adsorbents based on montmorillonite for contaminant removal from water: A review, Applied Clay Science

123:239-258.

[41] Vadivelan V, Kumar KV, Equilibrium, kinetics, mechanism, and process design for the sorption of methylene blue onto rice husk, J. Colloid Interface Sci. 286:90-100.

[42] Sun Y, Ding C, Cheng W, Wang X, Simultaneous adsorption and reduction of U (VI) on reduced graphene oxide-supported nanoscale zerovalent iron, J. Hazard. Mater. 280:399-408.

Figures

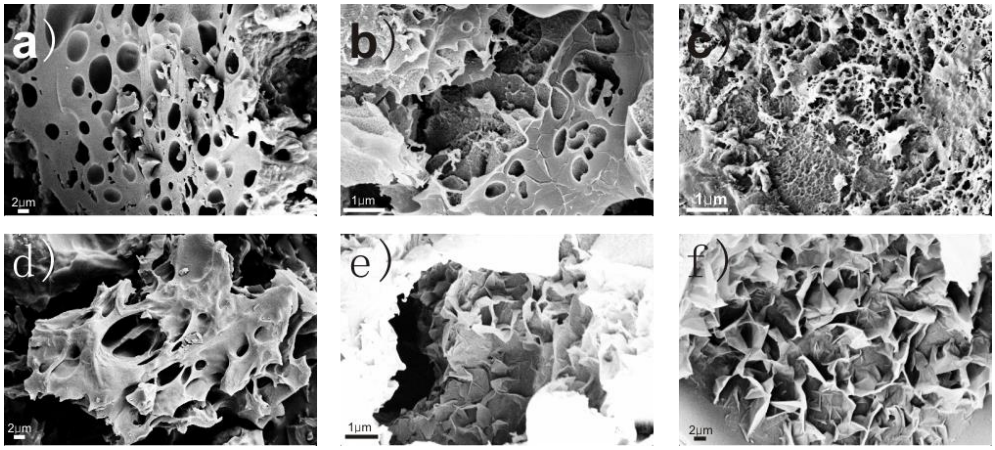

Fig. 1 SEM images of LS-AC-1, LS-AC-4, LS-AC-5, MS-AC-1, MS-AC-4 and MS-AC-5, respectively.

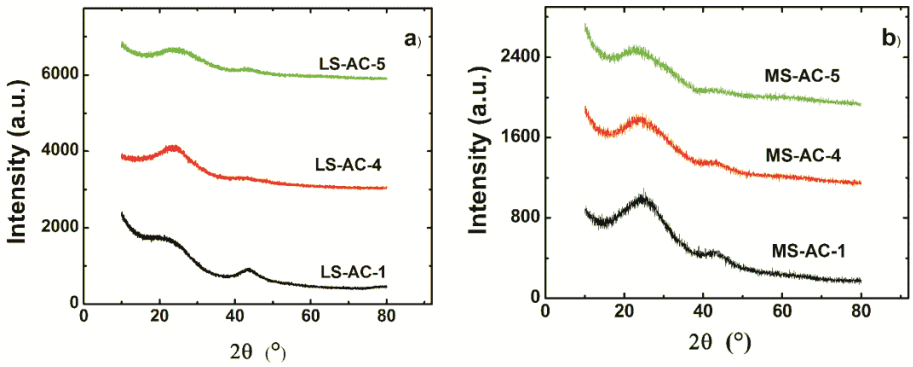

Fig. 2 XRD patterns of LS-AC-1, LS-AC-4, LS-AC-5, MS-AC-1, MS-AC-4 and MS-AC-5, respectively.

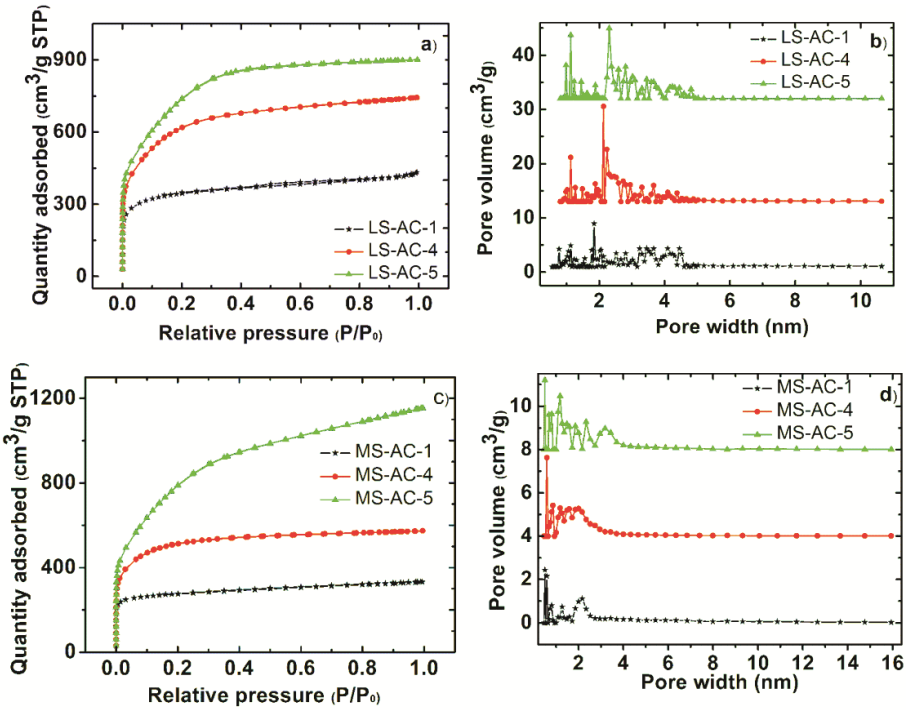

Fig. 3 Nitrogen adsorption-desorption isotherms (a, c) and pore size distribution (b, d) of longan seed and mangosteen skin derived porous carbons, respectively.

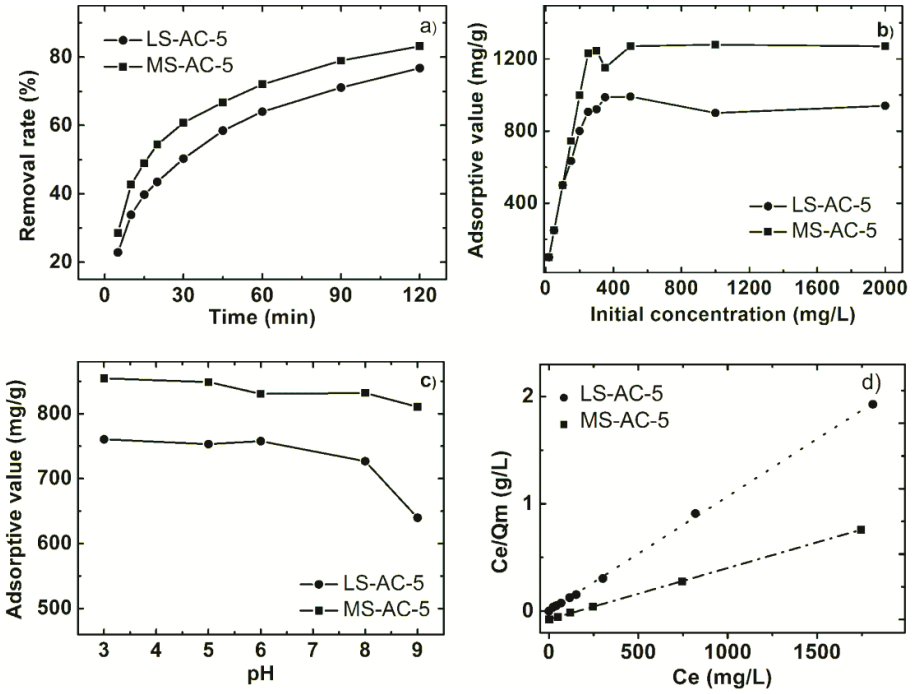

Fig. 4 a) Effect of contact time of LS-AC-5 and MS-AC-5 for Rhodamine-B adsorption; b) Adsorption isotherms of Rhodamine-B on LS-AC-5 and MS-AC-5, respectively; c) Effect of pH on the removal of Rhodamine-B by LS-AC-5 and MS-AC-5; d) Langmuir fitted curves.

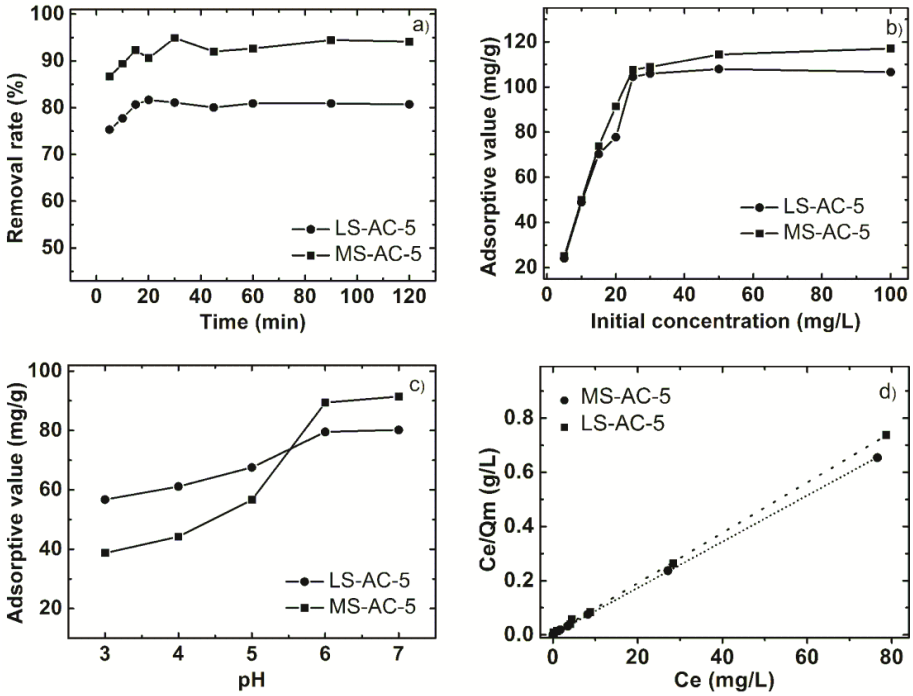

Fig. 5 a) Effect of contact time of LS-AC-5 and MS-AC-5 for Pb(II) ions adsorption; b) Adsorption isotherms of Pb(II) ions on LS-AC-5 and MS-AC-5, respectively; c) Effect of pH on the removal of Pb(II) ions by LS-AC-5 and MS-AC-5 ; d) Langmuir fitted curves.

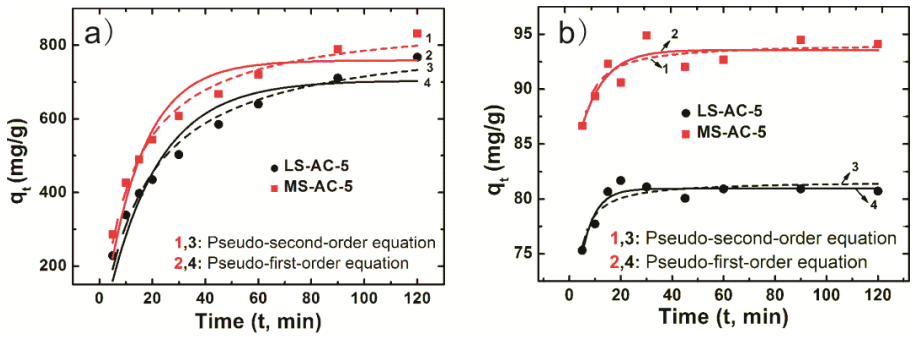

Fig. 6 Adsorption kinetics data and fitted models of a) Rhodamine-B and b) Pb(II) ions onto LS-AC-5 and MS-AC-5, respectively.

Tables:

Table 1 Specific surface area and pore structure of samples activated with different ratios of potassium hydroxide to biochar.

Samples	Surface area ($m^2.g^{-1}$)	Pore volume ($cm^3.g^{-1}$)	Average pore size (*nm*)
LS-AC -1	803.51	0.47	2.36
LS-AC -4	2038.74	1.15	2.09
LS-AC -5	2728.98	1.39	2.04
MS-AC -1	940.24	0.51	2.19
MS-AC -4	2188.30	1.19	2.01
MS-AC -5	2960.56	1.77	1.93

Table 2 Isotherm adsorption parameters Rhodamine-B and Pb(II) ions on MS-AC-5 and LS-AC-5, respectively.

Model	Langmuir model			Freundlich model		
	Q_m (*mg/g*)	K_L (*L/mg*)	R^2	*n*	K_F ($mg^{1-1/n}/g{\cdot}L^{1/n}$)	R^2
Pb(II) ions on LS-AC-5	107.53	2.04	0.9995	4.86	57.35	0.6735
Pb(II) ions on MS-AC-5	117.65	3.33	0.9999	7.19	78.26	0.8877
RB on LS-AC-5	1000.20	0.47	0.9994	12.44	322.14	0.4253
RB on MS-AC-5	1265.82	0.69	0.9999	6.26	522.91	0.4144

Table 3 Kinetic parameters for Rhodamine-B and Pb(II) ions adsorption on MS-AC-5 and LS-AC-5, respectively.

Kinetic model	Pseudo-first -order			Pseudo-second -order		
	k_1 (min^{-1})	q_e (*mg/g*)	R^2	k_1 (*g/mg·min*)	q_e (*mg/g*)	R^2
Pb(II) ions on LS-AC-5	0.5343	80.58	0.721	0.0309	81.65	0.813
Pb(II) ions on MS-AC-5	0.5338	92.67	0.529	0.0235	94.19	0.807
RB on LS-AC-5	0.0514	704.37	0.915	7.0968×10^{-5}	835.87	0.978
RB on MS-AC-5	0.0690	758.71	0.907	9.7796×10^{-5}	876.62	0.985